# Estimates of Ta strength at ultrahigh pressures and strain rates using thin-film graded-density impactors

J. L. Brown,[1] D. P. Adams,[1] C. S. Alexander,[1] J. L. Wise,[1] and M. B. Prime[2]
[1]*Sandia National Laboratories, Albuquerque, New Mexico 87185, USA*
[2]*Los Alamos National Laboratory, Los Alamos, New Mexico 87545, USA*

(Received 7 March 2019; revised manuscript received 21 May 2019; published 14 June 2019)

We present results from an experimental technique used to estimate the strength of Ta at extreme pressures (150 GPa) and strain rates ($10^7$ $s^{-1}$). A graded-density impactor (GDI) was fabricated using sputter deposition to produce an approximately 40-$\mu$m-thick film containing alternating layers of Al and Cu. The thicknesses of the respective layers are adjusted to give an effective density gradient through the film. The GDIs were launched with a 2-stage light gas gun, and shock-ramp-release velocity profiles were measured over timescales of ~10 ns. Results are presented for the direct impact of the film onto LiF windows, which allows for a dynamic characterization of the GDI, as well as from impact onto thin (~40$\mu$m) sputtered Ta samples backed by a LiF window. The measurements were coupled with mesoscale numerical simulations to infer the strength of Ta, and the results agree well with other high-pressure platforms, particularly when strain-rate, microstructural, and thermodynamic-path differences are considered.

DOI: 10.1103/PhysRevB.99.214105

## I. INTRODUCTION

Generating physics-based models that predict the deformation of materials under dynamic loading remains a long-standing challenge. Significant investments have been made to establish experimental capabilities that can probe relevant conditions. Modern high-pressure (>10 GPa), high-strain-rate (>$10^5$ $s^{-1}$) experiments generally fall into two categories: perturbation growth and release wave profile measurements. Perturbation growth experiments apply an acceleration to an interface with prescribed perturbations (typically sinusoidal) and monitor the subsequent growth. Early experiments utilizing explosive loading drove a Rayleigh-Taylor (RT) instability and observed sensitivity of the perturbation growth to dynamic strength [1]. More recently, RT experiments have been adapted to laser platforms for which similar sensitivities are observed [2,3]. This idea has also been extended to plate impact experiments in which the shock loading results in a Richtmyer-Meshkov instability (RMI); in this case, a methodology is prescribed to directly estimate the dynamic strength based on the observed perturbation growth [4]. The second category of experiment is release wave profile measurements. In these experiments, the deformation is restricted to one-dimensional uniaxial strain, and the dynamic compression path incorporates a release (or unloading) that drops the pressure from the peak state. Under these conditions, materials are observed through velocimetry to exhibit a transition between elastic and plastic deformation, and this transition can be related to the material strength. Experiments have been performed with plate impact configurations to shock-load a material prior to the release [5], as well as with magnetic loading to perform shockless (or ramp) compression and release [6].

One of the most well-studied materials against this backdrop is tantalum. Ta is a refractory metal that is predicted to remain in its initial body-centered-cubic (bcc) crystal structure to pressures of at least 1 TPa [13], making it a model material. A summary of the types of strength experiments that have been performed on Ta and some characteristic states associated with those experiments is given in Fig. 1. The most common data available are from quasistatic (QS) and split-Hopkinson bar (SHB) experiments [8]. In these tests, pressures are close to atmospheric conditions and accessible strain rates range from $10^{-3}$ to $10^{-1}$ $s^{-1}$ (QS) and $10^3$ to $10^4$ $s^{-1}$ (SHB). Diamond anvil cell experiments have been performed to explore Ta strength under high-pressure isothermal loading at strain rates comparable to the QS tests [9]. The difficulty and cost of performing higher-rate experiments make the remaining data rather sparse. Magnetic loading has been used to perform ramp compression and release experiments at rates of $\sim 3 \times 10^5$ $s^{-1}$ and to pressures of 250 GPa on the Z machine [10]. Higher-rate data come exclusively from perturbation growth techniques. RMI experiments probe high-rate (~$10^7$ $s^{-1}$) free-surface (zero pressure) conditions [7], while the laser RT experiments are conducted at similar rates but much higher pressures. RT data have been reported up to 130 GPa using the Omega laser [11,12] and up to 350 GPa using the National Ignition Facility (NIF) [3,11].

Significant questions arise when attempting to piece together the information in Fig. 1 into a comprehensive picture of material strength. Specifically, can the laser and magnetic-loading experiments be compared on a similar basis to distinguish between rate and pressure effects? Since the experimental methodologies are completely different, there is a need to perform release experiments in higher-strain-rate regimes to enhance the confidence with which we can make these types of cross-platform comparisons. Towards this end, we present an experimental capability that enables a shock-ramp-release dynamic compression path at loading rates on the order of ~$10^7$ $s^{-1}$. Sec. II describes the approach, in

 

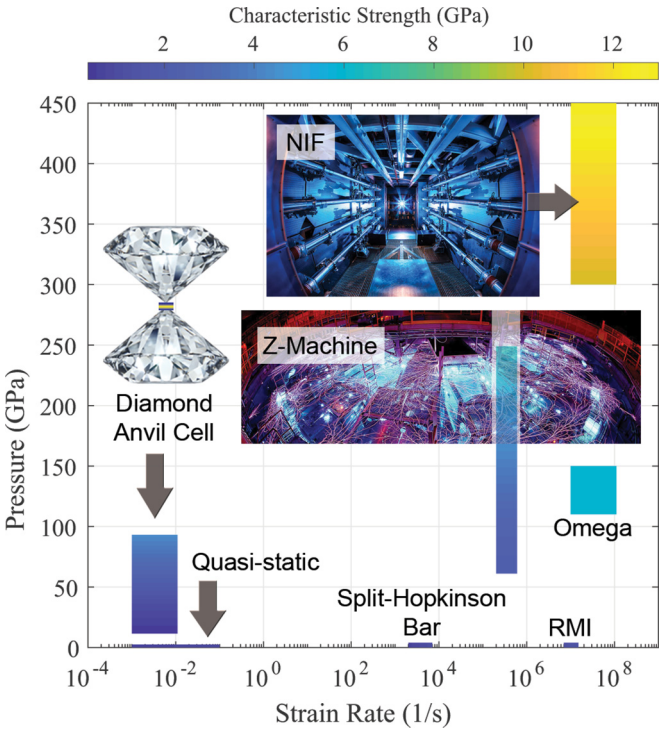


FIG. 1. Characteristic conditions for several Ta experimental data sets available in the literature, adapted from [7]. Quasistatic and split-Hopkinson bar experiments cover low-pressure, moderate-strain-rate conditions [8], and recent Richtmyer-Meshkov (RMI) techniques have extended to higher rates [7]. Diamond anvil cells can be used to access low-rate, high-pressure conditions [9]. Magnetic loading on the Z machine has been used to dynamically compress to high pressures at high rates [10], while laser platforms such as Omega [11,12] and NIF [3] have been used to access similar pressures at even higher rates.

which we fabricate a graded-density impactor (GDI) using thin-film deposition for use in plate impact experiments. A detailed explanation of the experimental configuration is given in Sec. III, followed by a description of a numerical simulation capability in Sec. IV. We present the experimental results, analysis, and subsequent discussion in Sec. V, and conclude in Sec. VI.

## II. MATERIALS FABRICATION

### A. Graded-density impactors

Graded-density impactors (GDIs) have long been recognized as a viable technique to perform ramp compression loading using plate impact gun systems [14]. GDIs utilize a continuous change in the impactor's shock impedance, such that impact results in a compressive wave with a rise time that can be orders of magnitude slower than the nearly instantaneous shock that is produced with a homogeneous impactor. Traditionally, the length scales associated with the GDIs that have been explored are $O$(mm) and the resulting timescales for the rise time of the ramp are $O(\mu s)$ [14,15]. In this section, we present a technique to fabricate GDIs that reduces these length and time scales two orders of magnitude to generate the desired loading rates of $10^7$ $s^{-1}$.

The key idea in our approach is to deposit hundreds of individual nanometer-scale layers of different materials to establish an effective density gradient through the thickness of the film. A bimetal system of Al and Cu is selected for this initial work because these materials contain a relatively large difference in shock impedance and each metal can be deposited at high rates while maintaining low residual film stresses (important for film adhesion and integrity). The GDI fabrication begins with the choice of a substrate. A low-impedance material is required to provide a release from the peak state, and we chose Al because it is easily diamond machined to provide an optimal coating surface. The substrates were 4 mm thick and 12.7 mm in diameter. Substrates were solvent cleaned and their surfaces were etched with Ar (100 W, 5 min) prior to sample loading in the deposition system.

A cryopumped, KDF 744i pulsed dc magnetron sputter deposition system having a base pressure of $10^{-5}$ Pa was utilized for GDI film deposition. A custom platen was designed such that tens of GDIs could be produced in a single deposition run. The deposition begins with a 25-nm-thick layer of Ti for improved substrate adhesion along with a 35-nm-thick layer of Ni for use as a diffusion barrier. It is desirable to have a thick high-impedance base layer to provide a steady peak state in the loading condition, so 5.5 $\mu$m of Cu was deposited on the diffusion barrier for this purpose. Next, the key feature of the GDI was applied: alternating layers of Cu and Al were deposited where each layer thickness was varied to give an effective gradient in density. This multilayer portion of the GDI can be envisioned as having 100 bilayers, where a bilayer is defined to be 1 Al layer and 1 Cu layer. The bilayer thickness is fixed at 340 nm throughout the multilayer deposition, and the thickness of the Al and the Cu within each bilayer was adjusted to give a 1% change in molar composition from the previous bilayer. Thus, the 100 bilayers (200 individual layers) result in a 34 $\mu$m deposition representing an effective change in composition from pure Cu to pure Al as the film growth proceeds. The GDI was then finalized by depositing a 2 $\mu$m Al cap, which is intended to produce a steady postshock state prior to the arrival of the ramp wave induced by the multilayer. Sputter deposition of the various layers involved filtered ultrahigh-purity (UHP) argon with flow controlled by an MKS Instruments 100 sccm mass flow controller. Ar pressure was set to 1.33 Pa for the deposition of each layer as indicated by an MKS capacitance gauge. Sputtering utilized Advanced Energy Pinnacle Plus power supplies operating in pulsed dc mode, and large (12 × 62.25 cm) sputter targets combined with programmed stage scanning established uniform layer thicknesses. Sputter target purities were as follows: Ti (99.995%), Ni (99.99%), Cu (99.995%), and Al (99.999%). Deposition rates were determined for each material prior to final GDI fabrication employing a calibrated DEKTAK surface profilometer and focused ion beam sectioning/scanning electron microscopy (SEM) for thickness measurements.

A few GDI films were locally sectioned by focused Xe ion beam sputtering and polished with a focused Ga ion beam to enable characterization using SEM. A representative GDI film is shown in Fig. 2. There is no detectable delamination, and this film appears to be free of gross contamination or particles. Individual layer thicknesses of GDIs have been

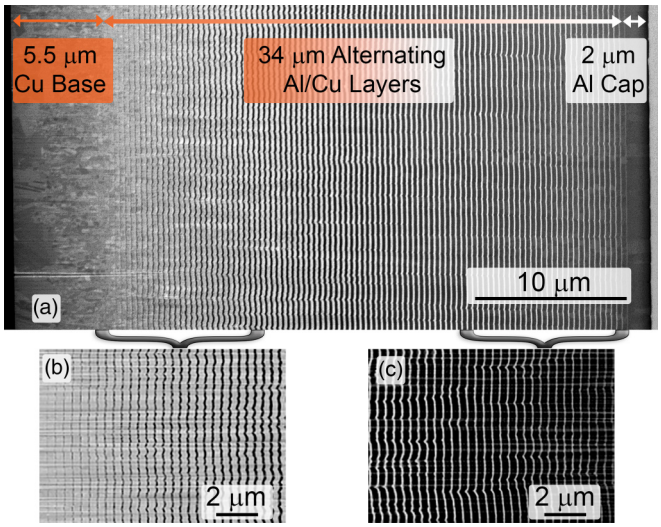


FIG. 2. SEM cross section view of the Cu/Al GDI with individual layers oriented vertically. The image in (a) shows the base Cu layer, graded multilayer, and Al cap. Images in (b) and (c) show Cu-rich and Al-rich portions of the multilayer, respectively. The Al layers appear dark while the copper layers are lighter.

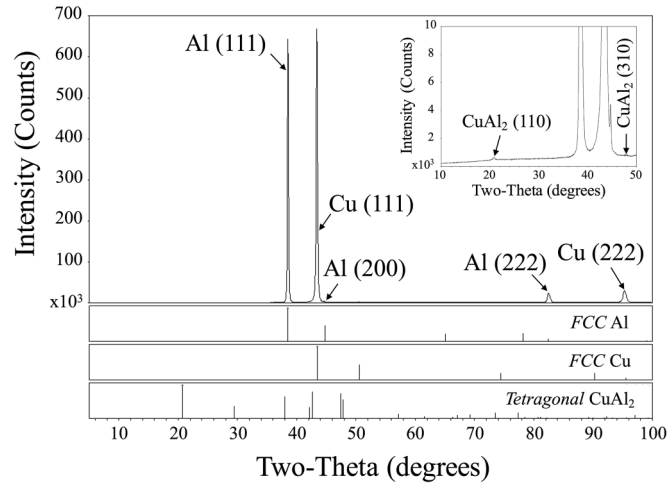


FIG. 3. Diffractogram obtained from sputter-deposited Cu/Al multilayer showing evidence for Cu, Al, and trace (<0.1 wt. % $CuAl_2$). The known reflections of candidate materials are displayed below the diffractogram.

measured and are within 5% of targeted values, confirming the desired composition profile. In addition, the measurements confirm that the bilayer thicknesses of the GDI (combined thickness of a single Al and single Cu layer) are constant and approximately equal to 340 nm, so the sputter process did not drift out of calibration during the lengthy deposition. Sections obtained from different substrates and locations contain no measurable differences, demonstrating excellent film thickness uniformity. Additionally, surface roughness measurements on GDI films using a white light interferometer reveal an average peak to valley of $0.5 \pm 0.1$ $\mu$m while optical profilometry suggests a planarity of $<1$ $\mu$m. These low values are comparable to the flatness and parallelism of the diamond-turned Al suggesting the film surface roughness is a result of conformal deposition onto the substrate and the deposition process does not contribute additional uncertainty to the interpretation of an impact experiment.

X-ray diffraction (XRD) shows that GDI films are mostly elemental, face-centered-cubic Cu and Al. A Siemens model D500 $\theta$-$\theta$ powder diffractometer (Bruker AXS, Inc., Madison, WI) was used for data collection with samples maintained at ambient temperature. Monochromatic Cu K$\alpha$ (0.15406 nm) radiation was produced using a diffracted-beam curved graphite monochromator. Fixed slits were used, and the instrument power settings were 40 kV and 30 mA. Datascan V4.3 (Materials Data, Inc., Livermore, CA) software was used to operate the diffractometer. Phase identification was performed using the Jade 9.6 software package (Materials Data, Inc., Livermore, CA) coupled with the 2018 Powder Diffraction File PDF-4+ (ICDD, Newtown Square, PA).

Diffractograms reveal intense reflections for Cu and Al. Both exhibit a (111) out-of-plane crystallographic texture. The diffractogram shown in Fig. 3 was obtained from a separate thin-film sample specifically deposited for XRD study (but not used for impact studies). Identical deposition parameters were used with one exception. The film characterized in Fig. 3 did not contain the relatively thick Al capping layer. This portion was skipped in order to fabricate a sample that could be probed sufficiently by x rays that penetrate to several buried interfaces within the multilayered volume. Trace Cu-Al intermetallic was detected only by inspecting near the noise floor of the diffractogram as shown in the Fig. 3 inset plot. XRD shows evidence for small amounts of $CuAl_2$ that likely form at Cu/Al interfaces. Based on observed peak intensities obtained in the scan, the amount of $CuAl_2$ is estimated to be less than 0.1 wt. %. Quantification of weight percent phases was performed using reference intensity ratio values obtained from the PDF database along with the EASY QUANT routine within the Jade software.

### B. Tantalum targets

Tantalum films used as targets in high-velocity impact experiments were deposited using a separate turbomolecular-pumped Unifilm PVD 300 multisource sputter deposition system. This other vacuum system maintained a base pressure of $2 \times 10^{-5}$ Pa. LiF (100) substrates were initially cleaned using an *ex situ* plasma etcher (100 W, Ar) and then loaded into the deposition system for coating. LiF was first coated with a 20-nm-thick layer of Ti followed by ~43-$\mu$m-thick Ta. Filtered UHP Ar was maintained at a pressure of 11 mTorr for sputtering. This pressure was chosen based on a series of preliminary experiments that examined the residual stress of deposited Ta on LiF using traditional wafer curvature methods. These initial experiments involved deposition of 10-$\mu$m-thick surrogate films onto 4-mm-thick LiF substrates at different, fixed Ar pressures. Wafer curvature was measured before and after film growth using a Toho FLX wafer curvature apparatus and film stress was determined using Stoney's equation (working within the thin-film approximation). Again, film thickness was determined using a calibrated DEKTAK surface profilometer (with ride-along witness samples) and focused ion beam sectioning/SEM.

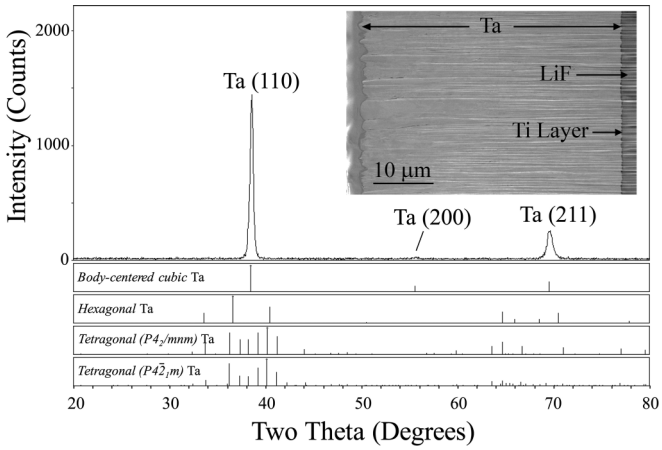


FIG. 4. Diffractogram obtained from sputter-deposited Ta thin film demonstrates a body-centered cubic structure. The reflections associated with several candidate Ta structures are included below the diffractogram. A cross section scanning electron micrograph of Ta thin film on LiF substrate showing the full thickness is provided as the inset. The film was locally coated with Pt to minimize rounding of exposed Ta film surface during focused-ion-beam sectioning. The horizontal lines observed in this image are mostly artifacts introduced as part of the sectioning process.

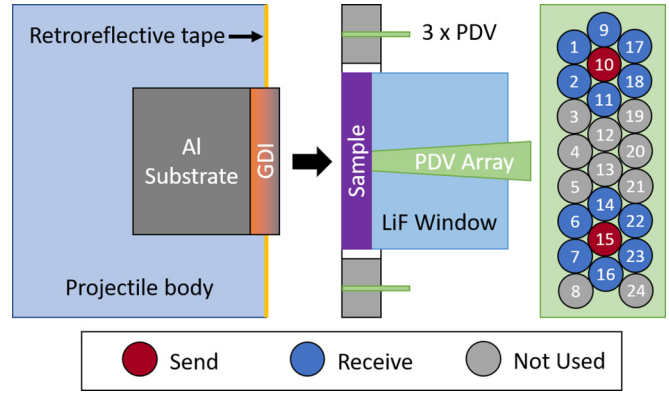


FIG. 5. Plate impact experiment configuration. The GDI impacted a sample of interest (either 5 $\mu$m of Al or 43 $\mu$m of Ta) and PDV was used to measure both the impact velocity and the velocity of the sample/LiF window interface. A PDV array was used to measure the velocity of 12 distinct spots across ~1 mm to provide the statistics necessary to obtain the required precision in the sample velocity.

Tantalum films used as targets in GDI experiments were 43 $\mu$m thick, on average. An example cross section micrograph of a thick Ta film is shown in Fig. 4. Tantalum films developed a columnar microstructure having facets at the final surface characterized by a peak-to-valley surface roughness of ~2$\mu$m. Grain widths increased slightly as the film was thickened with widths as large as ~3 $\mu$m. XRD revealed a body-centered-cubic (bcc) structure in Ta films. The x-ray diffractogram in Fig. 4 shows several reflections; each matches well the known reflections of bcc Ta. Other candidate phases and their diffraction patterns are included below the diffractogram for comparison. A bcc structure is expected when employing Ti adhesion layers [16,17]. Tantalum films had a fiber texture with most grains having a (110) and (211) out-of-plane orientation aligned to the LiF (100) substrate normal. The diffraction methods used for Ta film characterization are similar to those described for GDI characterization.

## III. EXPERIMENTAL CONFIGURATION

Experiments were performed using the two-stage light gas gun at the Shock Thermodynamics Applied Research (STAR) facility at Sandia National Laboratories [18]. This gun launches 25.4-mm-diameter projectiles at velocities of 2–7 km/s. The target configuration utilized a standard transmitted wave plate impact orientation, a cartoon of which is shown in Fig. 5. The 12.7-mm-diameter GDIs were glued into the projectiles such that ~1 mm was protruding from the surface and retroreflective tape was applied to the remaining surface of the projectile. Sample materials were deposited directly onto 19-mm-diameter and 4-mm-thick [100] LiF windows and then potted into an Al target plate. Samples were either 5-$\mu$m-thick Al or 43-$\mu$m-thick Ta (as described in Sec. II); the choice of these materials and thicknesses is discussed further in Sec. V.

### Velocimetry diagnostic

Photonic Doppler velocimetry (PDV) [19] was utilized during testing. Three standard collimating PDV probes (AC Photonics) were located 120 deg apart along a 21 mm diameter. These probes were used to accurately measure the velocity of the projectile by monitoring 1550 nm laser light returned from the retroreflective tape. The primary measurement of interest is the velocity of the sample/LiF interface. The challenge in this measurement is the timescale associated with the thin-film GDIs. As will be shown in Secs. IV and V, the timescale of the ramp generated with these GDIs is on the order of 5 ns. This is comparable to dynamic experiments performed on laser platforms [20,21] where, traditionally, a line-imaging velocity interferometer using a streak camera is used to obtain the necessary temporal resolution [22]. As this type of imaging system was not available for these experiments, we pursued PDV measurements for this purpose. The STAR PDV system utilizes 20 GHz photodetectors and digitizers ranging in bandwidth from 12 to 23 GHz. This corresponds to system rise times of ~20–30 ps, which is more than sufficient to observe the features of interest in these experiments. A set of preliminary experiments was conducted using several common PDV configurations [23] incorporating either collimating or bare-fiber probes coupled to diffuse or specular reflecting surfaces. In general, we found the bare-fiber probes coupled to a specular surface gave the best signal quality, but the signals were still too inconsistent to be useful. As a result, we utilized a probe obtained from Berkshire photonics that incorporates a tight packing of an 8 × 3 array of SMF-28 fibers into a 2.1-mm-diameter steel tube. The fiber core diameters are 9 $\mu$m while the outer cladding diameter is 125 $\mu$m, giving a spacing of ~1 mm across the fibers. The philosophy with this probe was to make as many redundant measurements as possible and use statistical averaging to provide the required

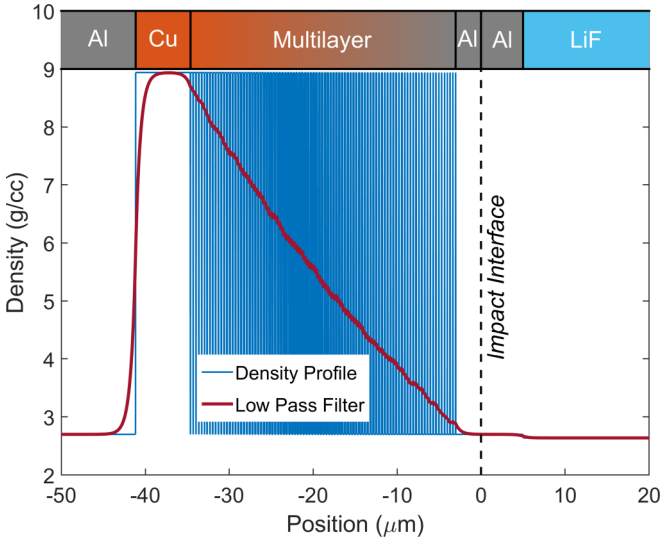


FIG. 6. Initial (time = 0) spatial density profile for the direct numerical simulation of a GDI impact showing each distinct layer of Al and Cu. The low-pass filter was applied as a visual aid representing the average density gradient through the GDI.

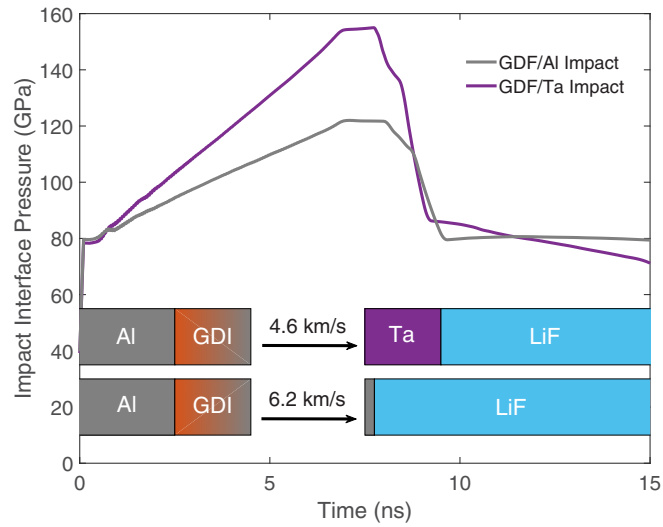


FIG. 7. Simulated pressure histories at the interface between the GDI and either a thin (5 $\mu$m) Al or thick Ta (43 $\mu$m) sample. Impact velocities were tailored to give the same initial shock pressure.

precision. Due to limitations in the availability of oscilloscope channels, only 12 PDV measurements were taken; a schematic of the arrangement is shown in Fig. 5. The probe was glued directly to the back of the LiF window, and fibers numbered 10 and 15 were used to illuminate the Al or Ta reflecting surface with 1550 nm laser light. The six probes surrounding the points of illumination were used to collect the reflected light before being coupled (with a 3 GHz upshift) into the PDV system.

## IV. NUMERICAL SIMULATIONS

Simulations of the experiments were performed using the ALEGRA hydrocode [24]. A significant advantage of this GDI approach is the use of full density layers of well-known materials. The GDI profile shown in Fig. 2 was imported directly into ALEGRA to provide a mesoscale simulation capability. The simulations were configured using a 1-D Lagrangian mesh in which 10 elements were constructed over the smallest layer thickness and then mass matched across the domain, resulting in cell sizes of 0.47 nm or 1.56 nm across the Al or Cu elements, respectively. The equations of state were modeled with the Sesame 3700 [25] and 3325 tables and the Steinberg-Cochran-Guinan form was used to model the strength [26]. A plot of the initial (time = 0) spatial configuration is shown in Fig. 6 that illustrates the density differences across the GDI (discrete layers of Al and Cu) and into the Al sample and LiF window. A low-pass filter was applied to give a visual representation of the average density gradient through the alternating layers of the GDI.

Time histories of the simulated pressures at the impact interface for impacts of 4.6 and 6.2 km/s on Ta and Al, respectively, are shown in Fig. 7. These profiles illustrate the desired features of an initial shock with a steady hold, ramp to the peak state with a steady hold, and a release back down to a lower pressure. We note the timescale for this entire experiment is only ~10 ns, which is about 2 orders of magnitude faster than conventional GDI techniques [14,15].

## V. EXPERIMENTAL RESULTS AND ANALYSIS

Four experiments were conducted, which are summarized in Table I. The experiments were performed in pairs where a thin-Al-sample experiment was followed by a separate thick-Ta experiment and the impact velocities were coordinated so the initial shock stresses were as close as possible (as in Fig. 7). This pair of experiments was chosen such that the first (Al) provides a drive characterization while the second is used to infer the Ta strength. The drive characterization would ideally consist of an impact directly on the LiF window, but the thin Al coating was used to provide a reflecting surface and shield the measurement from any gas traveling ahead of the projectile. The simulations described in Sec. IV confirm that the nearly identical shock impedance between Al and LiF at these pressures results in minimal wave interactions and so this configuration is still well suited to dynamically quantify the behavior of the GDI.

Spectrograms along with 95% confidence intervals on the extracted velocities (shown as the shaded regions) obtained from 4 of the 12 fibers (labeled in Fig. 5) in the PDV array from experiment GDI-1 are shown in Fig. 8(a). This subset was chosen to represent the best and the worst measurements and illustrates some qualitative trends common across the entire experimental series. The signal quality appears to be completely random and can vary drastically between different fiber locations. Signal dropouts also seem to be completely uncorrelated and occur at random times. However, by making 12 redundant measurements we consistently obtain several high-quality signals.

Rather than selecting the best signal, we chose to statistically average all 12 signals to provide the best estimate of the velocity. This was done by first shifting each signal such that the initial shocks overlap. The shock arrivals have

TABLE I. Summary of the GDI experiments.

| Shot Number | Sample | Impact Velocity (km/s) | Impact Stress (GPa) | Peak Stress (GPa) |
|---|---|---|---|---|
| GDI-1 | 5 $\mu$m Al | 6.179 | 80 | 122 |
| GDI-2 | 43 $\mu$m Ta | 4.055 | 78 | 151 |
| GDI-3 | 5 $\mu$m Al | 4.608 | 53 | 80 |
| GDI-4 | 43 $\mu$m Ta | 3.010 | 52 | 99 |

a spread of ∼5 ns in the raw data due to impactor tilt and slight differences in the fiber lengths, so using the shock as a fiducial was preferable to a detailed accounting of these sources of timing differences. This assumption is justified by the excellent spatial uniformity of the GDI described in Sec. II. Next, a weighted average of the signals was taken in which the weights were given by the reciprocal of the known variance in each measurement. In practice, this weighting results in regions of the signals with high noise (such as dropouts) contributing very little to the average, and so the highest-quality signals naturally dominate the averaging. The estimated errors associated with this averaging are ∼20 m/s, which is sufficient for an accurate wave speed analysis [27]. The averaged velocities after additionally correcting for the index of refraction of LiF [28] are given in Fig. 8(b). The velocity detected before the shock arrival on GDI-1 and GDI-3 is hypothesized to be gas blow-by traveling ahead of the projectile prior to impact. This small perturbation is believed to be overdriven by the strong shock in the Ta experiments (where it does not appear) and so this feature does not influence the interpretation of the data.

### A. Drive determination

The Al sample experiments (GDI-1 and GDI-3) can be used to perform a dynamic characterization of the loading history provided by GDI. This was done by coupling the numerical simulations described in Sec. IV to the measured experimental velocities. The idea is to use the simulations to describe the thermodynamic differences between the drive characterization impact and the Ta sample impact. The experiments were designed such that the initial impact pressures were nearly the same; as shown in Fig. 7, the state of each impact is nearly identical at early times. At later times, the wave interactions within the GDI reflect off the higher-impedance Ta sample, causing higher pressures and a divergence between the two loading conditions. If we assume that the simulations accurately calculate this divergence, then a mapping can be constructed to describe the difference between the loading on the thin Al sample and the loading on the Ta sample. We use the transfer function methodology described in Ref. [6]. Briefly, this is a linear perturbation theory approach in which a transfer function, TF, can be constructed in the frequency domain using a fast Fourier transform (FFT) and the simulated

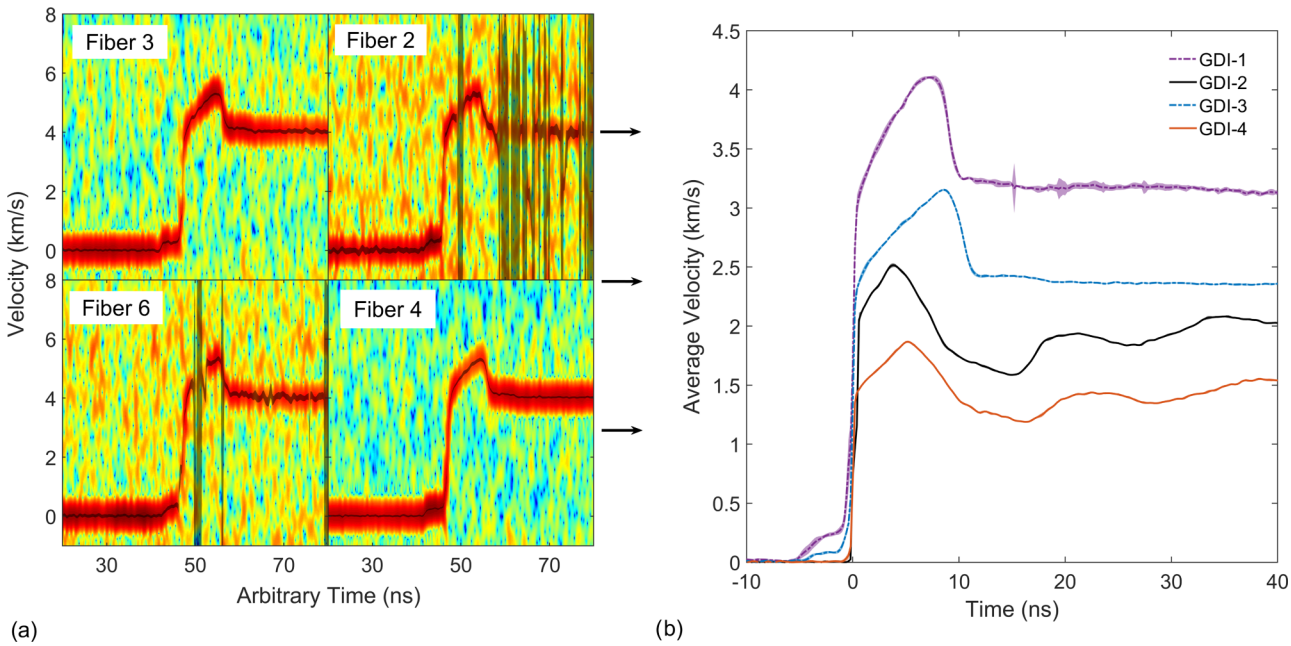


FIG. 8. The subset of the 12 measured PDV spectrograms in (a) represents the range of signal quality, where the gray shaded regions represent the 95% confidence intervals on the velocity extraction (which visually collapse to a line in regions of high signal quality). After aligning the initial shocks to time = 0, the estimated variance for each signal is used to produce (b), the weighted averaged velocity for each experiment. Shaded regions represent the 95% confidence intervals in the mean velocity, although they are mostly indistinguishable from the linewidth.

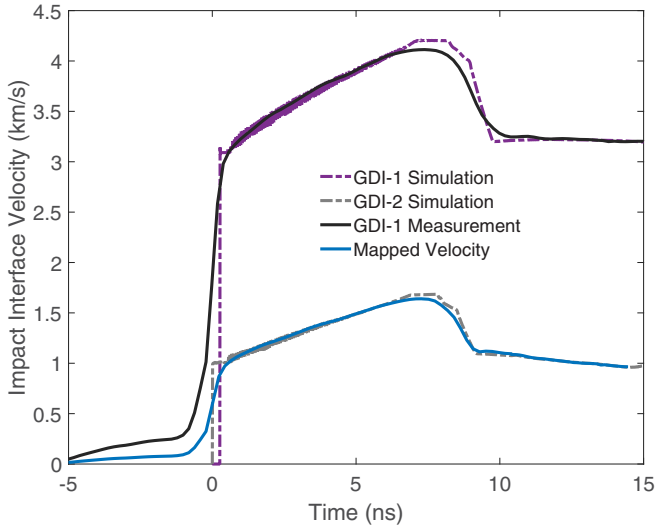


FIG. 9. Drive calculation for experiments GDI-1 and GDI-2. The differences between the GDI-1 drive characterization simulation and experiment are linearly mapped to the simulated loading velocity in the GDI-2 Ta simulation.

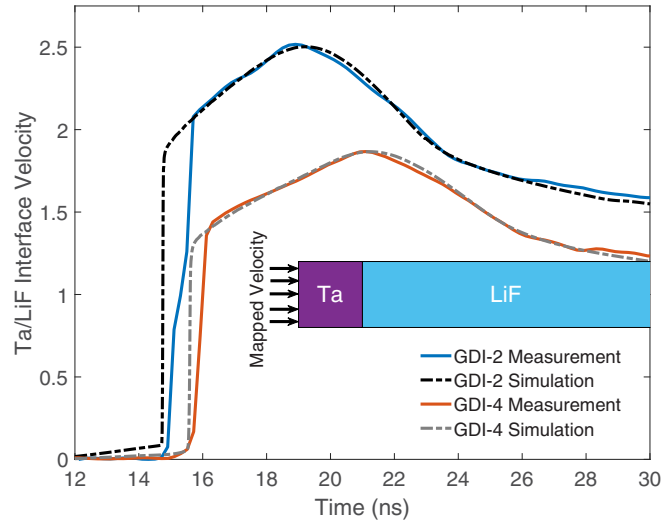


FIG. 10. Best-effort simulations for the Ta experiments using the mapped velocity boundary condition shown in Fig. 9. The Ta EOS is assumed known and determines the time shift in the experimental data, giving the excellent agreement in the postshock ramp.

velocities, $u_{\mathrm{Al}}$ and $u_{\mathrm{Ta}}$:

$$\mathrm{TF}(\omega) = \frac{\mathrm{FFT}(u_{\mathrm{Al}})}{\mathrm{FFT}(u_{\mathrm{Ta}})}. \tag{1}$$

With the TF constructed using the simulated velocities, it can then be applied [through the inverse of Eq. (1)] to the measured velocity in the Al experiment to generate an estimate of the time history of the velocity at the impact interface in the Ta experiment. This mapping is illustrated in Fig. 9, where the GDI-1 and GDI-2 simulated profiles are used to generate the TF. Subsequently, the TF is applied to the GDI-1 measurement to generate the mapped velocity profile.

### B. Wave speed analysis

Once the velocity-time history at the impact interface in the Ta sample experimental configuration has been calculated, it can then be used as a boundary condition to drive 1-D simulations to aid in the analysis of the Ta experiment. Reconsider the simulation configuration in Fig. 6 in which the entire GDI is replaced by the mapped velocity applied directly as the input to the sample (illustrated as the cartoon in Fig. 10). Ta simulations were conducted using the Sesame 93524 equation of state (EOS) [29] coupled to the Preston-Tonks-Wallace (PTW) strength model [30] and an anelastic description of the release [31]. This anelastic model was used previously to model shock-release measurements in Ta [39], and only a slight empirical tuning of those reported parameters was required to capture our experiments. The simulation results are shown in Fig. 10 for which there is excellent agreement between simulation and experiment in the critical region following the initial shock. As in the drive determination (Fig. 9), the initial shock in the measurements is more dispersive than the simulations. Since the rise times in the measurements are consistent across the high-quality signals, we do not believe this is an artifact from the averaging across multiple fibers. Instead, we attribute this difference to a deficiency in the simulation, such as a problem with the artificial viscosity (which was tuned only to the minimum required to remove instabilities in the initial shock). However, because this modeling discrepancy is accounted for through the TF analysis, we do not believe it alters our interpretation of the experiment.

We note that a time shift has been applied to the experimental measurement to obtain consistency with the postshock-ramp wave. We believe this is a reasonable approximation because the EOS has been well studied [10,27] over these conditions and so it can be used to constrain this time shift. Once this level of agreement between simulation and experiment has been obtained, the methodology described in [6,10] can be used to determine the wave speed response shown in Fig. 11. The loading wave speed, by construction, is in good agreement with the estimated postshock-ramp compression path. The unloading portion of the wave speed represents the measured transition from elastic to plastic deformation and agrees well with the magnetically driven ramp-release experiments performed under similar thermodynamic paths at the Z machine [10]. This transition is sensitive to the deviatoric response of the material and can be used to estimate properties related to strength [6]. The inset in Fig. 11 contains the simulated equivalent plastic strain rate halfway into the Ta sample for both experiments. The high-rate initial shock is followed by the ramp at a strain rate of $\sim 10^7$ s$^{-1}$. Upon reversal of the loading (peak of the velocity profile), the rate drops to zero and then increases again as the plastic strain begins to accumulate upon release. The unloading strain rate is remarkably similar to the loading rate, which is an ideal scenario in these types of experiments.

### C. Ta strength estimates

The wave speed profiles in Fig. 11 can be used to obtain estimates of the shear modulus, $G$, at peak compression as well as the average strain $\epsilon$, and change in shear stress, $\Delta\tau$,

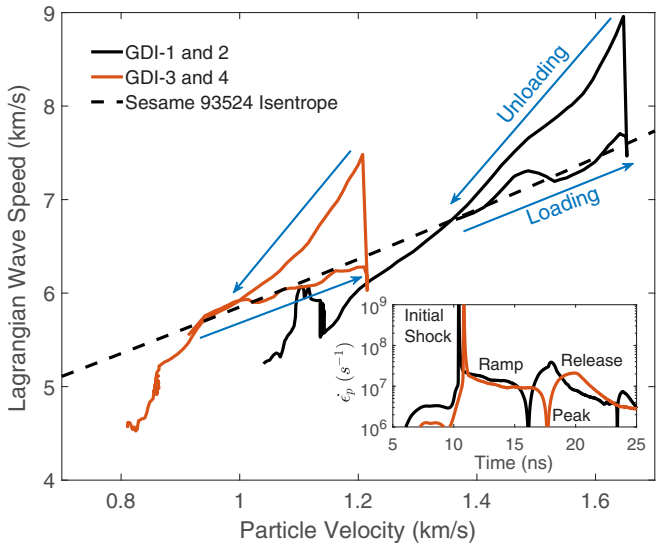


FIG. 11. The analysis methodology described in [6,10] is used to determine the Lagrangian wave speed as a function of particle velocity. The initial loading was constrained to agree with the 93524 Sesame EOS, while the unloading represents the elastic-plastic transition that is dictated by the Ta strength response. The inset contains the simulated equivalent plastic strain rates as a function of time halfway into the Ta sample.

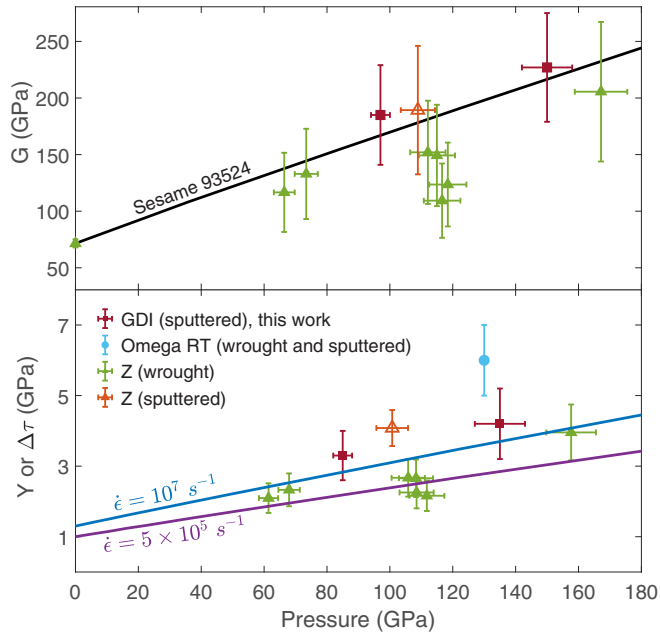


FIG. 12. Shear modulus ($G$) and change in shear stress ($\Delta\tau$) estimated from the wave speed profiles shown in Fig. 11. Data from ramp-release experiments on Z [10] and laser RT experiments on Omega [2,11] are shown for comparison. The strain rate curves in the lower panel are based on the zero-pressure interpolation between split-Hopkinson bar [8] and RMI [7] data and a $G/G_0$ pressure scaling based on the Sesame 93524 $T = 0$ shear modulus.

during the elastic-plastic unloading transition [6]. The results of this analysis are given in Table II and shown in Fig. 12. Uncertainties were estimated using the Monte Carlo approach described in [10] in which uncertain parameters are sampled according to a prescribed normal distribution and the analysis is repeated for each instantiation to obtain statistics on the strength estimates. Prescribed uncertainties were 1 $\mu$m on the Ta thickness, 2% scaling of the velocity boundary condition, 30% in the simulated flow stress, and 20% in the anelastic parameters. These uncertainties result in full coverage: the 95% confidence intervals in the simulated velocities completely encompass the experimental measurements. We find the resulting uncertainties in the strength estimates are dominated by the errors in the thickness and boundary conditions with little contribution from the model parameters, which is consistent with the assumptions in the analysis [6]. Figure 12 also contains a reanalysis (using a nonlinear LiF index of refraction [28]) of the Z experiments from [10] as well as the laser driven (Omega) RT experiments from [11,12]. As illustrated, the results are in excellent agreement with previous work. The shear modulus agrees well with both the Z experiments and the Sesame 93524 cold shear modulus. The strength appears to be slightly higher than the Z experiments but lower than the Omega data (although just overlapping in the error bars).

TABLE II. Summary of the strength estimates. Uncertainties represent 1 standard deviation. The first pressure entry is the average over the elastic-plastic transition while the second is the peak value.

| Shot Number | $P$ (GPa) | $\Delta\tau$ (GPa) | $G$ (GPa) | $\epsilon$ |
|---|---|---|---|---|
| GDI-1/2 | $135, 150 \pm 8$ | $4.2 \pm 1$ | $227 \pm 48$ | $0.294 \pm 0.010$ |
| GDI-3/4 | $85, 97 \pm 3$ | $3.3 \pm 0.7$ | $185 \pm 44$ | $0.234 \pm 0.005$ |

### D. Discussion

In this section, we discuss the differences in Fig. 12 in relation to estimated physical effects due to the discrepancies between the experiments. Specifically, we examine the differences between loading rate, loading path, and microstructure.

As shown in Table III, the different experimental platforms result in different characteristic timescales and subsequent strain rates. The GDI gun experiments in this work and the laser-driven Omega experiments are estimated to result in comparable strain rates ($\sim 10^7$ s$^{-1}$) while the magnetically driven Z experiments are 1.5 orders of magnitude lower. To estimate the effect of rate on strength between these experiments we begin by examining zero-pressure experimental data. Split-Hopkinson bar experiments suggest a strength of $\sim$0.55 GPa at room temperature and a compressive strain rate of 1300 s$^{-1}$ [8], while the RMI experiments have an inferred

TABLE III. Differences between the experimental platforms shown in Fig. 12.

| Experiment | Shock Pressure (GPa) | Shock Temperature (K) | Strain Rate (s$^{-1}$) |
|---|---|---|---|
| GDI (this work) | 80 | 1220 | $10^7$ |
| Omega [11,12] | 50 | 660 | $10^7$ |
| Z [10] | | | $3 \times 10^5$ |

strength of $\sim 1.3 \pm 0.1$ GPa at an average strain rate of $\sim 1.2 \times 10^7$ s$^{-1}$ [7]. A linear interpolation (in log space) to the Z experimental strain rates suggests an equivalent Z experiment at 0 pressure should have a strength of ~1 GPa. We note that these experiments utilize the same lot of well-characterized Ta plate [32], so we expect this interpolation to be reasonable. To assess the pressure scaling, we make the assumption common to many strength models [26,33] that the material strength scales linearly with the shear modulus: $Y = Y_0 \frac{G}{G_0}$. Using the Sesame 93524 cold shear modulus (shown in Fig. 12 to be a reasonable representation of the data), curves representing the pressure-dependent strength for the characteristic rate for each experiment can be constructed. These curves, which are shown in Fig. 12, are consistent with the measured differences between the majority of the Z and GDI experiments.

The differences in the thermodynamic loading path are primarily due to the different initial shock magnitudes. Since shock hardening has been shown to have a minimal effect on the dynamic loading of Ta [34], we focus here on temperature differences. As show in Table III, the GDI experiments contain the largest initial shock, the Omega experiments are slightly lower, and the Z experiments are completely shockless. Thus, the GDI experiments can be viewed as starting on a higher-temperature adiabat. Using the principal Hugoniot from the Sesame 93524 table, the GDI experiments are estimated to be ~660 K hotter than the Omega experiments and ~920 K hotter than the Z experiments. Examination of the solidus in the 93524 table, however, reveals that these temperatures are not a significant fraction of the melt temperature. At a pressure of 80 GPa, for instance, melt corresponds to a temperature of $T_m = 5750$ K. Thus, Ta is not expected to experience significant thermal softening in any of these experiments. The temperature effect on the shear modulus can be assessed through the model used to simulate the GDI experiments [30,35]: $G(\rho, T) = G(\rho)(1 - 0.21 \frac{T}{T_m(\rho)})$. This model suggests a minimal change to shear modulus (<5%) and subsequent strength. We note that we are not considering any of the plastic work heating or additional contributions to thermal softening, but a detailed accounting for these contributions does not change the nature of this conclusion. The simulations described in Sec. V B, for example, result in a thermal softening of 0.3 GPa (7.5% on 4 GPa).

The final difference of note between the three experiments is microstructure. In the interest of platform development, we chose to sputter the Ta directly onto the LiF windows in the GDI experiments to avoid glue bonds. The Omega experiments consist of both wrought and sputtered samples (a single average is reported), while the majority of the Z experiments contain wrought material but a sputtered sample was also examined. The same lot of material was used in both sets of wrought experiments and the Z sputtered sample was intended to mimic the Omega samples in the interest of a coordinated cross-platform validation. The Ta films in the GDI experiments were described in Sec. II and had a microstructure comparable to the Omega and Z sputtered samples. Curiously, the Z experiments suggest the sputtered sample is ~30% stronger than the wrought material, but no observable difference is observed in the Omega data. The expected strengthening according to the Hall-Petch (HP) scaling is reviewed in [36]; for Ta $\Delta\tau \propto \frac{k}{\sqrt{d}}$, where $k = 0.76$ GPa $\mu$m$^{1/2}$ and $d$ is the grain size. The wrought and sputtered samples are estimated to have grain sizes of 24 $\mu$m [32] and 0.25 $\mu$m [12], respectively, resulting in a strength increase of ~1.4 GPa, which is consistent with the Z data. Conversely, Park *et al.* postulate that the reason no HP scaling is observed in their experiments is that the geometrically necessary dislocation (GND) generation that typically describes the HP effect is minimal under the high-rate deformation of laser loading rates [12,37]. This theory is also consistent with the Z data, where the GND strengthening at the Z experimental rates is close to what was estimated using the simple HP scaling [37]. The GDI experiments are most consistent with the Z wrought data, particularly when considering the strain rate differences. Thus, the GDI experiments suggests there is not significant grain size strengthening, which offers further support to the GND hypothesis.

In summary, comparisons can be made between the GDI, Omega, and Z experiments by examining differences in the initial microstructure, thermodynamic path, and loading rate. Estimates of these effects suggest excellent agreement between the GDI and Z experiments, but the Omega data remain an outlier. Since the GDI and Z experiments utilize the same ramp-release approach to measuring strength, while the Omega experiments utilize the RT instability methodology, the most likely explanation is that there may be platform dependencies that influence how the experimental observables are interpreted to estimate material strength.

Complicating factors can enter both types of experiments. In the instability experiments, for example, extraction of quantitative strength information requires a methodology to couple the experimental measurements to simulation, so the results inherently depend on this methodology. In the release experiments, questions arise with how the extracted quantities are generalized to strength. Strain-rate-induced relaxation and wave attenuation can introduce systematic errors [38], particularly in the inferred shear modulus. Similarly, complexities in deformation mechanisms during reverse loading can alter the observed properties [39–41].

## VI. CONCLUSIONS

We have developed an experimental platform to study material strength at high-pressure and high-strain-rate conditions. A GDI technique was utilized to perform shock-ramp-release experiments and velocimetry was used to measure the time history of the subsequent wave profile. The GDI was fabricated using a sputter deposition methodology in which alternating layers of Al and Cu were deposited at the nanometer length scale to produce a smooth density gradient over a 34-$\mu$m-thick film. Initial experiments were performed on sputtered Ta samples resulting in initial shock pressures of 50–80 GPa followed by a ramp to peak pressures of 100–150 GPa at rates of $10^7$ s$^{-1}$. The release wave profile was used to infer shear moduli of 155–190 GPa and strengths of 3–4 GPa near these peak states. The strength estimates are consistent with the shear modulus scaling to high pressure as well as similar magnetic loading [10] experiments, but are lower than what is inferred from laser RT experiments [11,12]. A systematic examination of the differences between

these experimental platforms, including loading rate, loading path, and microstructure, suggests there could be platform dependencies that complicate the interpretation of these high-rate, high-pressure experiments.

## ACKNOWLEDGMENTS

The authors would like to thank C. Sobczak, M. A. Rodriguez, J. Michael, and B. Farfan for technical assistance. We also appreciate the insightful discussions with T. Mattsson and W. Reinhart. This work was supported by the Laboratory Directed Research and Development program at Sandia National Laboratories, a multimission laboratory managed and operated by National Technology and Engineering Solutions of Sandia, LLC, a wholly owned subsidiary of Honeywell International, Inc., for the US Department of Energy's National Nuclear Security Administration under Contract No. DE-NA-0003525.

[1] J. F. Barnes, P. J. Blewett, R. G. McQueen, K. A. Meyer, and D. Venable, Taylor instability in solids, J. Appl. Phys. **45**, 727 (1974).

[2] H. S. Park, B. A. Remington, R. C. Becker, J. V. Bernier, R. M. Cavallo, K. T. Lorenz, S. M. Pollaine, S. T. Prisbrey, R. E. Rudd, and N. R. Barton, Strong stabilization of the Rayleigh-Taylor instability by material strength at megabar pressures, Phys. Plasmas **17**, 056314 (2010).

[3] B. A. Remington, H.-S. Park, D. T. Casey, R. M. Cavallo, D. S. Clark, C. M. Huntington, C. C. Kuranz, A. R. Miles, S. R. Nagel, K. S. Raman, and V. A. Smalyuk, Rayleigh-Taylor instabilities in high-energy density settings on the National Ignition Facility, Proc. Natl. Acad. Sci. USA (2018).

[4] M. B. Prime, W. T. Buttler, M. A. Buechler, N. A. Denissen, M. A. Kenamond, F. G. Mariam, J. I. Martinez, D. M. Oró, D. W. Schmidt, J. B. Stone, D. Tupa, and W. Vogan-McNeil, Estimation of metal strength at very high rates using free-surface Richtmyer-Meshkov instabilities, J. Dyn. Behav. Mater. **3**, 189 (2017).

[5] J. R. Asay and J. Lipkin, A self-consistent technique for estimating the dynamic yield strength of a shock-loaded material, J. Appl. Phys. **49**, 4242 (1978).

[6] J. L. Brown, C. S. Alexander, J. R. Asay, T. J. Vogler, and J. L. Ding, Extracting strength from high pressure ramp-release experiments, J. Appl. Phys. **114**, 223518 (2013).

[7] M. B. Prime, W. T. Buttler, S. J. Fensin, D. R. Jones, R. Manzanares, D. T. Martinez, J. I. Martinez, D. K. Schmidt, and C. P. Trujillo, Tantalum strength at extreme strain rates from impact-driven Richtmyer-Meshkov instabilities (unpublished).

[8] S. R. Chen and G. T. Gray, Constitutive behavior of tantalum and tantalum-tungsten alloys, Metall. Mater. Trans. A **27**, 2994 (1996).

[9] A. Dewaele and P. Loubeyre, Mechanical properties of tantalum under high pressure, Phys. Rev. B **72**, 134106 (2005).

[10] J. L. Brown, C. S. Alexander, J. R. Asay, T. J. Vogler, D. H. Dolan, and J. L. Belof, Flow strength of tantalum under ramp compression to 250 GPa, J. Appl. Phys. **115**, 043530 (2014).

[11] H. S. Park, N. R. Barton, J. L. Belof, K. J. M. Blobaum, R. M. Cavallo, A. J. Comley, B. R. Maddox, M. J. May, S. M. Pollaine, S. T. Prisbrey, B. A. Remington, R. E. Rudd, D. W. Swift, R. J. Wallace, M. J. Wilson, A. Nikroo, and E. Giraldez, Experimental results of tantalum material strength at high pressure and high strain rate, in *Shock Compression of Condensed Matter—2011: Proceedings of the Conference of the American Physical Society Topical Group on Shock Compression of Condensed Matter*, edited by M. L. Elert, W. T. Buttler, J. P. Borg, J. L. Jordan, and T. J. Vogler, AIP Conf. Proc. No. 1426 (American Institute of Physics, Melville, NY, 2012), p. 1371.

[12] H. S. Park, R. E. Rudd, R. M. Cavallo, N. R. Barton, A. Arsenlis, J. L. Belof, K. J. M. Blobaum, B. S. El-dasher, J. N. Florando, C. M. Huntington, B. R. Maddox, M. J. May, C. Plechaty, S. T. Prisbrey, B. A. Remington, R. J. Wallace, C. E. Wehrenberg, M. J. Wilson, A. J. Comley, E. Giraldez, A. Nikroo, M. Farrell, G. Randall, and G. T. Gray, Grain-Size-Independent Plastic Flow at Ultrahigh Pressures and Strain Rates, Phys. Rev. Lett. **114**, 065502 (2015).

[13] P. Soderlind and J. A. Moriarty, First-principles theory of Ta up to 10 mbar pressure: Structural and mechanical properties, Phys. Rev. B **57**, 10340 (1998).

[14] L. M. Barker, High-pressure quasi-isentropic impact experiments, in *Shock Compression of Condensed Matter*, edited by J. R. Asay, R. Graham, and G. Straub (Elsevier Science Publishers, 1984), p. 217.

[15] S. J. Yep, J. L. Belof, D. A. Orlikowski, and J. H. Nguyen, Fabrication and application of high impedance graded density impactors in light gas gun experiments, Rev. Sci. Instrum. **84**, 103909 (2013).

[16] S. Sato, Nucleation properties of magnetron-sputtered tantalum, Thin Solid Films **94**, 321 (1982).

[17] E. A. I. Ellis, M. Chmielus, and S. P. Baker, Effect of sputter pressure on Ta thin films: Beta phase formation, texture, and stresses, Acta Mater. **150**, 317 (2018).

[18] J. R. Asay, The Sandia National Laboratories Shock Thermodynamics Applied Research (STAR) Facility, Report No. SAND81-1901, Sandia National Laboratories, 1981.

[19] O. T. Strand, D. R. Goosman, C. Martinez, T. L. Whitworth, and W. W. Kuhlow, Compact system for high-speed velocimetry using heterodyne techniques, Rev. Sci. Instrum. **77**, 083108 (2006).

[20] D. C. Swift and R. P. Johnson, Quasi-isentropic compression by ablative laser loading: Response of materials to dynamic loading on nanosecond time scales, Phys. Rev. E **71**, 066401 (2005).

[21] R. F. Smith, J. H. Eggert, R. E. Rudd, D. C. Swift, C. A. Bolme, and G. W. Collins, High strain-rate plastic flow in Al and Fe, J. Appl. Phys. **110**, 123515 (2011).

[22] P. M. Celliers, D. K. Bradley, G. W. Collins, D. G. Hicks, T. R. Boehly, and W. J. Armstrong, Line-imaging velocimeter for shock diagnostics at the omega laser facility, Rev. Sci. Instrum. **75**, 4916 (2004).

[23] B. J. Jensen, D. B. Holtkamp, P. A. Rigg, and D. H. Dolan, Accuracy limits and window corrections for photon doppler velocimetry, J. Appl. Phys. **101**, 013523 (2007).

[24] A. Robinson, T. Brunner, S. Carroll, R. Drake, C. Garasi, T. Gardiner, T. A. Haill, H. Hanshaw, D. Hensinger, D. Labreche, R. Lemke, E. Love, C. Luchini, S. Mosso, J. Niederhaus, C. Ober, S. Petney, W. Rider, G. Scovazzi, O. Strack, R. Summers, T. Trucano, V. Weirs, M. Wong, and T. Voth, ALEGRA: An arbitrary Lagrangian-Eulerian multimaterial, multiphysics code, in *Proceedings of the 46th AIAA Aerospace Sciences Meeting and Exhibit* (American Institute of Aeronautics and Astronautics, Inc., Reston, VA, 2008).

[25] G. I. Kerley, Theoretical equation of state for aluminum, Int. J. Impact Eng. **5**, 441 (1987).

[26] D. J. Steinberg, S. G. Cochran, and M. W. Guinan, A constitutive model for metals applicable at high-strain rate, J. Appl. Phys. **51**, 1498 (1980).

[27] J.-P. Davis, J. L. Brown, M. D. Knudson, and R. W. Lemke, Analysis of shockless dynamic compression data on solids to multi-megabar pressures: Application to tantalum, J. Appl. Phys. **116**, 204903 (2014).

[28] J.-P. Davis, M. D. Knudson, L. Shulenburger, and S. D. Crockett, Mechanical and optical response of [100] lithium fluoride to multi-megabar dynamic pressures, J. Appl. Phys. **120**, 165901 (2016).

[29] C. W. Greeff, S. D. Crockett, S. P. Rudin, and L. Burakovsky, Limited Range Sesame EOS for Ta, Report No. LA-UR-17-22600, Los Alamos National Laboratories, 2017.

[30] S. K. Sjue and M. B. Prime, Starck Ta PTW strength model recommendation for use with SESAME 93524 EoS, Report No. LA-UR-17-21681, Los Alamos National Laboratory, 2017.

[31] J. N. Johnson, R. S. Hixson, G. T. Gray III, and C. E. Morris, Quasielastic release in shock-compressed solids, J. Appl. Phys. **72**, 429 (1992).

[32] T. Buchheit, E. K. Cerreta, L. Deibler, and S. Chen, Characterization of Tri-Lab Tantalum Plate, Report No. SAND2014-17645, Sandia National Laboratories, 2014.

[33] D. L. Preston, D. L. Tonks, and D. C. Wallace, Model of plastic deformation for extreme loading conditions, J. Appl. Phys. **93**, 211 (2003).

[34] D. H. Lassila and G. T. Gray, Effects of shock prestrain on the dynamic mechanical behavior of tantalum, J. Phys. IV (France) **1**, C3-19 (1991).

[35] L. Burakovsky, C. W. Greeff, and D. L. Preston, Analytic model of the shear modulus at all temperatures and densities, Phys. Rev. B **67**, 094107 (2003).

[36] Z. C. Cordero, B. E. Knight, and C. A. Schuh, Six decades of the Hall-Petch effect: A survey of grain-size strengthening studies on pure metals, Int. Mater. Rev. **61**, 495 (2016).

[37] R. E. Rudd, H. S. Park, R. M. Cavallo, A. Arsenlis, D. A. Orlikowski, S. T. Prisbrey, C. E. Wehrenberg, and B. A. Remington, Modeling of grain size strengthening in tantalum at high pressures and strain rates, in *Shock Compression of Condensed Matter - 2015: Proceedings of the Conference of the American Physical Society Topical Group on Shock Compression of Condensed Matter*, AIP Conf. Proc. No. 1793 (AIP, New York, 2017).

[38] A. P. Moore, J. L. Brown, H. Lim, and J. M. D. Lane, Verification of experimental dynamic strength methods with atomistic ramp-release simulations, Phys. Rev. Mater. **2**, 053601 (2018).

[39] J. N. Johnson, R. S. Hixson, D. L. Tonks, and G. T. Gray III, Shock compression and quasielastic release in tantalum, in *Highpressure science and technology—1993.*, edited by S. C. Schmidt, J. W. Shaner, G. A. Samara, and M. Ross, AIP Conf. Proc. No. 309 (AIP, New York, 1994), p. 1095.

[40] N. R. Barton, M. Rhee, and J. L. Brown, Modeling the constitutive response of tantalum across experimental platforms, in *Shock Compression of Condensed Matter - 2017: Proceedings of the Conference of the American Physical Society Topical Group on Shock Compression of Condensed Matter*, edited by R. Chau, T. C. Germann, J. M. D. Lane, E. N. Brown, J. H. Eggert, and M. D. Knudson, AIP Conf. Proc. No. 1979 (AIP, New York, 2018).

[41] M. Sliwa, D. McGonegle, C. Wehrenberg, C. A. Bolme, P. G. Heighway, A. Higginbotham, A. Lazicki, H. J. Lee, B. Nagler, H. S. Park, R. E. Rudd, M. J. Suggit, D. Swift, F. Tavella, L. Zepeda-Ruiz, B. A. Remington, and J. S. Wark, Femtosecond X-Ray Diffraction Studies of the Reversal of the Microstructural Effects of Plastic Deformation during Shock Release of Tantalum, Phys. Rev. Lett. **120**, 265502 (2018).